This is the Pre-Published Version.

S. Wang, P. Ding, S. Lin, X. Huang*, A. Usmani (2020) *Deformation of Wood in Fire: The Interaction between Heterogeneous Chemistry and Thermomechanical Stress*, **Proceedings of the Combustion Institute**, https://doi.org/10.1016/j.proci.2020.08.060

Deformation of Wood Slice in Fire: Interactions between Heterogeneous Chemistry and Thermomechanical Stress

Supan Wang[a, b], Pengfei Ding[a], Shaorun Lin[b], Xinyan Huang[b, *], Asif Usmani[b]

[a] *College of Safety Science and Engineering, Nanjing Tech University, Nanjing, 210009, China*

[b] *Research Centre for Fire Engineering, Department of Building Services Engineering, The Hong Kong Polytechnic University, Kowloon, Hong Kong*

*Correspond to xy.huang@polyu.edu.hk

Abstract

Wood is a common flammable material in the building fire and the dominant fuel in the wildland fire. In this work, disc wood slices were examined under irradiation to characterize the smoldering burning and the corresponding deformation behaviors. Due to interactions between chemical reactions and thermomechanical stresses, four successive deformation stages were observed and hypothesized: (I) drying shrinkage to ∪ shape, (II) irradiation-driven thermal expansion to ∩ shape, (III) pyrolysis shrinkage to ∪ shape, and (IV) oxidation-driven thermal expansion to ∩ shape. For these 5-15 mm thick samples, the degree and occurrence of these deformation stages are sensitive to the aspect ratio (i.e. D/δ). Increasing the slice thickness decreases the deformation in the first three stages but increases the deformation of the fourth stage. These experimental observations are qualitatively reproduced by a 2-D finite-element numerical model, coupling 3-step heterogeneous kinetics with a thermomechanical solver. Modeling results further verified the underlying heterogeneous processes (dehydration, pyrolysis, and oxidation) and thermomechanical stresses (thermal expansion and pre-stress) for each deformation stage. This study helps understand the influence of burning processes on the deformation of wood and the failure of timber structures.

Keywords: Timber; Charring; Smoldering; Thermal expansion; Finite element analysis; Aspect ratio

1. Introduction

Wood has been widely used for home decoration parts, furniture, and non-load bearing structural components, because of its visual attractiveness, durability, high strength-to-weight ratio, and renewable nature [1,2]. However, the fire risk of timber structures is still a primary safety concern, due to its flammable nature and large fuel loads [3–6], especially for high-rise timber buildings [7]. Wood is also the dominant fuel in the wildland fire. Burning wood particles (firebrands or embers) can transport downwind to start numerous new ignition spots and fires in the wildland-urban interface (WUI) [8]. In the literature, many studies have explored the combustion characteristics of the wood particles in the [9–18], and the influences of particle shape and size [9–11], oxygen supply [12–14] and heating conditions [15–19]. As a typical charring material, wood particles can sustain both forms of flaming and smoldering [20–22], but most of the literature focused on the flaming fire behaviors while the smoldering of wood particles due to heterogeneous chemistry is still not fully understood.

On the other hand, limited studies have looked into the deformation and failure of wood under mechanical loading and the thermal expansion under external heating [23–26]. Hori and Wada [24] found that the wood cellulose crystals had a linear thermal expansion below 180 °C and a faster expansion from 180 to 250 °C. Lineham *et al.* [27] studied the structural response of cross-laminated timber beams under structural loads and fire impact. Under external radiation, the formation of macro-

crack patterns was observed on the pyrolyzing thick wood blocks, which was caused by the thermomechanical induced surface wrinkling or buckling [25,26]. Recently, the structural and thermal properties of wooden materials, as well as their fire resistance and durability for building applications are reviewed [5,6]. However, to the best of authors' knowledge, few studies have addressed the burning and deformation behaviors during the smoldering wood fire, and the detailed interactions between heterogeneous chemistry and thermomechanical stress are still unclear.

In this work, we first conducted experiments on small-scale disc wood particles to investigate the deformation behaviors during smoldering under irradiation. The temperature and mass-loss rate during the whole ignition and smoldering processes are measured, and then interactions between burning and deformation characteristics are analyzed. Afterward, numerical simulations are performed to reveal more detailed heterogeneous physicochemical processes and structure responses, as well as verify the hypothesized governing mechanisms for different deformation stages.

2. Experiment

2.1 Experiment setup

In this work, typical beech wood slices were tested, which were cut perpendicular to the grains. All samples were first oven-dried at 80 ℃ for 8 h and then stored in the temperature and humidity chamber. Before the test, the circular wood slice was measured to have a density of 621 ± 21 kg/m^3 and moisture content of 10 ± 1 % at an ambient temperature of 300 K and relative humidity of 80%. Nine slice samples with three diameters (D) of 25 mm (small), 40 mm (medium) and 60 mm (large), and thickness (δ) of 5 mm (thin), 10 mm (medium) and 15 mm (thick) were tested. Their initial mass ranges from 1.6 ± 0.1 g to 25.8 ± 0.6 g.

Fig. 1 shows the schematic diagram of the experimental setup, which consists of a panel radiator, sample holder, and a precision scale. The 0.2 m × 0.2 m radiator panel was placed 50-mm above the wood slice, which provided uniform irradiation up to 60 kW/m^2 on the wood top surface. Before the test, the irradiation could be varied by adjusting the heating power and calibrated by a radiometer. The center point of the wood slice was glued with a 0.2-mm-diameter aluminum rod stick, which acted as a sample holder. Afterward, it was placed for 5 hours to stabilize the glued connection between the stick and the sample. The deformation degree of the wood slice can be expressed by the rotation (θ), as shown in Fig. 1(b), where the *positive* and *negative* values represent the deformation towards ∪ (or bowl) shape and ∩ (or umbrella) shape, respectively.

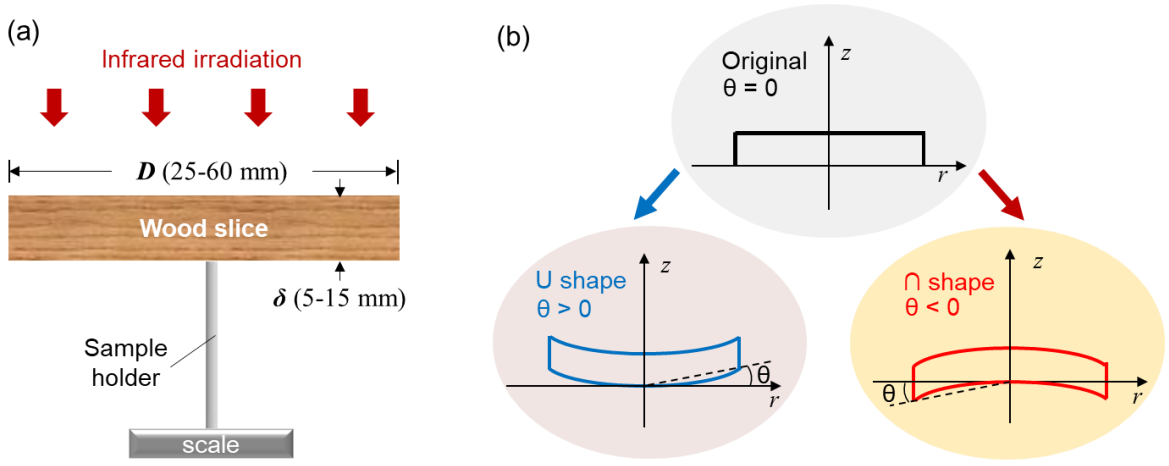

Fig. 1. Schematic diagram of (a) the experimental setup for the smoldering ignition and combustion of disc wood slice under irradiation, and (b) deformation process and rotation angle (θ) of disc sample.

Throughout the experiment, the irradiation level was fixed to be 20 ± 1 kW/m^2, which was strong enough to initiate a smoldering ignition [10,20]. The mass evolution of the wood sample was measured by the electric balance (Mettler-Toledo XE10002S, resolution: 0.01 g). The top and bottom surface temperatures of wood were carefully monitored using two 0.1-mm K-type thermocouples, whose extension wires were not in contact with the sample to avoid any interruptions. A video camera (Sony FDR-AX60 at 50 fps) was placed to record the burning and deformation phenomena. At least two experiments were conducted for each type of sample.

2.2. Burning and deformation phenomena

Fig. 2 shows the ignition and burning processes of large wood slices with the same diameter of 60 mm and two different thicknesses of 5 mm and 15 mm. Once heated by the irradiation, the sample started to release some visible smoke, most likely the water vapors and pyrolysis gases. Continuing the heating, glowing was always first visualized at the sample edge, because of the edge and curvature effects [10,28]. Afterward, the intensity of the smoke flow clearly increased, and occasionally smoke could eject from the crack. As a thicker layer of char and ash was formed on the top, the smoke flow reduced until burnout. Throughout the burning, there were four different deformation stages, and the 5-mm thick sample in Fig. 2(a) is used as an example. To reveal interactions between burning and deformation characteristics, Fig. 3 shows the detailed deformation evolution (θ), mass flux ($\dot{m}''$), and the temperature difference (ΔT) between the top and bottom surfaces.

(I) Drying shrinkage to ∪ shape. Once exposed to the irradiation, the wood top surface slightly shrunk, so that the sample deformed upward to form a ∪ shape. Such a deformation process occurred in the first 60 s and peaked at 27 s (Fig. 3a). The first deformation peak corresponded to the first peak mass flux due to drying, and maximum temperatures of the top surface (218 °C) and bottom surface (70 °C) were lower than the pyrolysis point (250-300°C [29–31]). Therefore, the drying shrinkage causes the deformation in this stage.

There are two possible reasons for such drying shrinkage, (1) the water introduced volumetric tension force is reduced by removing the bound water, and (2) the material stiffness is increased from the wet wood to dry wood. Both processes can result in the upward bend to form a ∪ shape. The dominant mechanism cannot be determined in the experiment but can be further verified by the subsequent numerical simulation (Section 3).

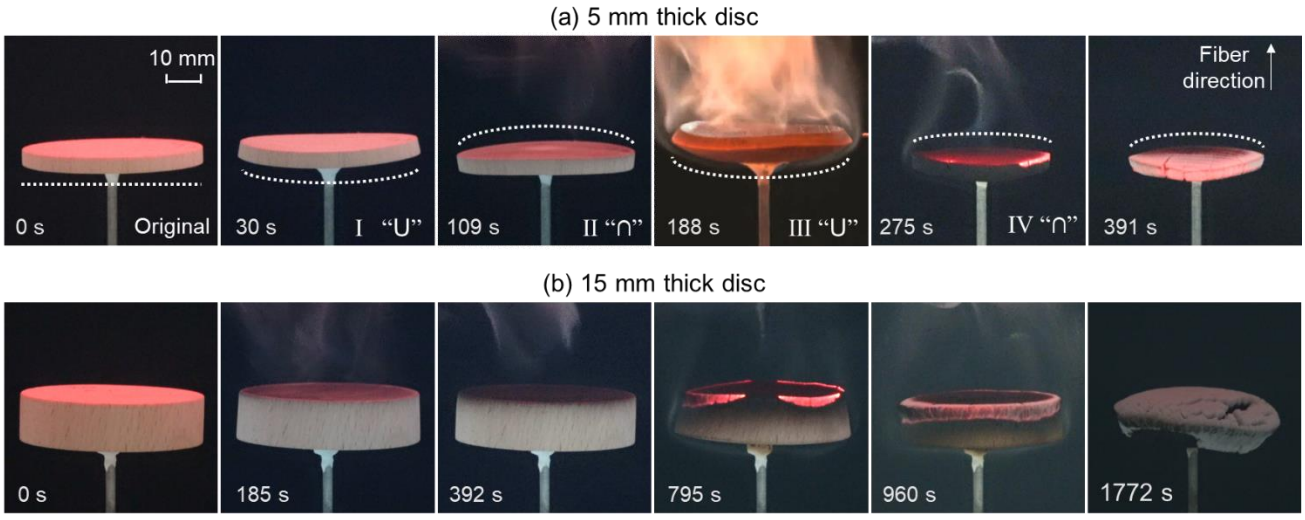

Fig. 2. Snapshots of heating process of large wood slices with a diameter of 60 mm and the thickness of (a) 5 mm (Video S1) and (b) 15 mm (Video S2).

(II) Thermal expansion to ∩ shape driven by external radiation. Then, the sample gradually bent back to the original flat shape at about 60 s, and then continuously deformed to a ∩ shape. As shown in Fig. 3(a), the maximum deformation of ∩ shape occurred at about 90 s and coincided with the minimal mass loss rate between two peak values. During Stage II, the temperature difference was stable near 175 °C, and the maximum temperature of the top surface was 270 °C that approached the pyrolysis point. Due to the temperature gradient caused by external radiation, the expansion of the hot top surface occurred first, which was more significant than cool bottom surface. Thus, different degrees of thermal expansion between the top and bottom surfaces promoted the deformation into ∩ shape.

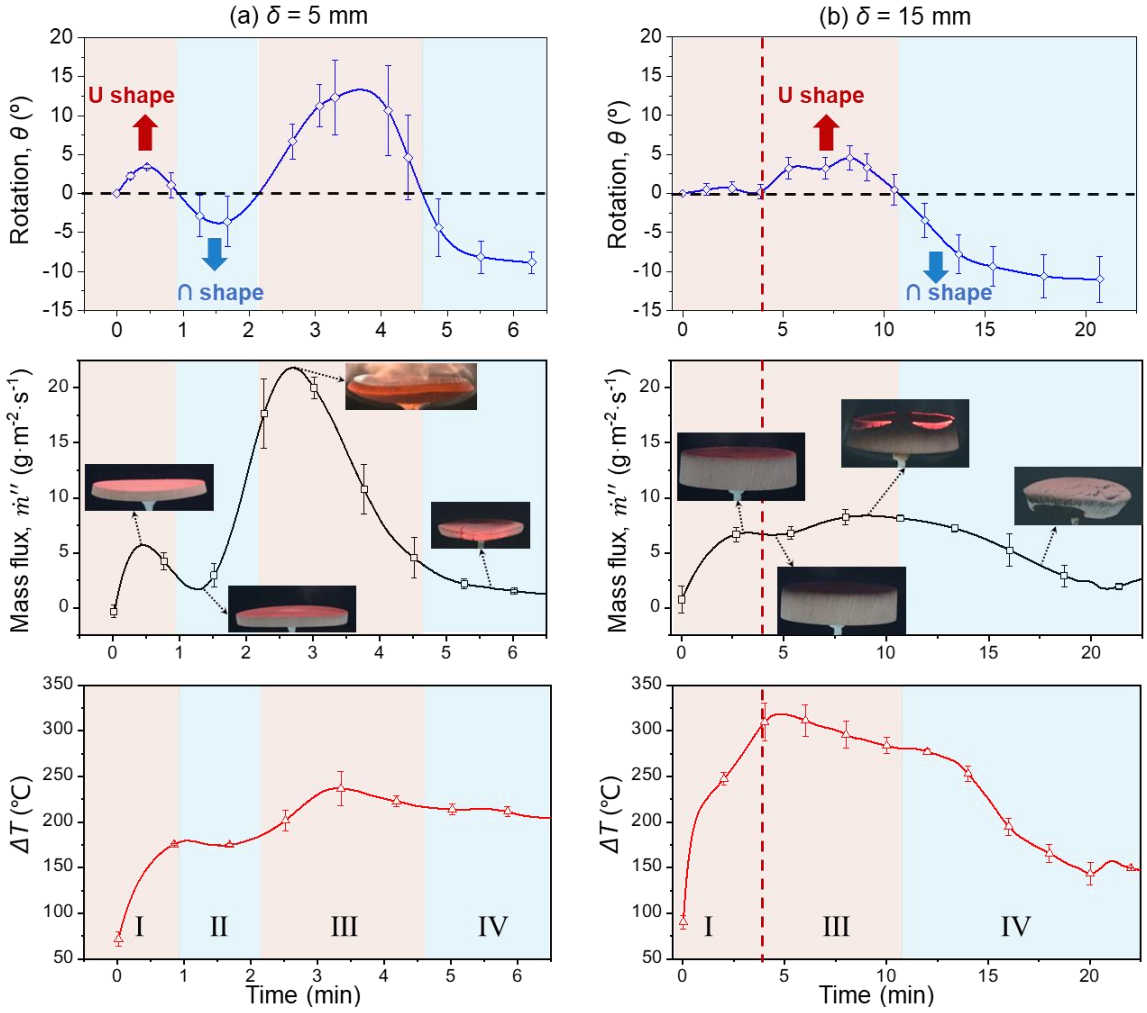

Fig. 3. Time evolution of rotation (θ), mass flux, and surface temperature difference in the smoldering process of 60-mm-diameter samples, where the various shading zones represent the different deformations during smoldering.

(III) Pyrolysis shrinkage to ∪ shape. Afterward, as the temperature quickly exceeded the pyrolysis point, the ∩-shaped deformation gradually transitioned to another ∪ shape. During the second ∪-shaped deformation, the largest rotation occurred at about 188 s, which was almost corresponded to the second peak mass flux in Fig. 3(a). At this maximum deformation point, the top and bottom surface temperatures were about 400 °C and 170 °C, respectively. Therefore, the formation of the second ∪ shape was mainly caused by the mass loss on the top surface due to strong pyrolysis (or charring) that converted the wood to the more porous char and resulted in a pyrolysis/charring shrinkage. Note that no crack of char surface was observed, different from thicker wood blocks in [25,26]. It was because

the non-uniform thermal stress inside the current thin slice was released through the deformation, which prevented the formation of cracks.

(IV) Thermal expansion to ∩ shape driven by char oxidation. After the wood fully pyrolyzed into char, the wood sample continued to smolder, and the char further oxidized into ashes. As the ash layer accumulated on the top surface, the char oxidation slowed down, and the mass-loss rate decreased. The temperature difference decreased, as the smoldering front propagated downward. The sample bent back to the original flat shape, and then continued to bend downward and deformed to another ∩ shape. Like the previous ∩ shape in Stage II, it could also be caused by the greater thermal expansion on the hotter top surface. Nevertheless, the upper surface was mainly heated by the exothermic char oxidation, whereas the external radiation was largely shielded by the ash layer. When approaching burnout, cracks occurred on the top ash layer, because of weak adhesion between ash particles.

As the slice thickness increased to 15 mm (Fig. 3b), the overall deformation degree was weaker. Before clear charring and pyrolysis, the wood slice was almost flat, although there was a clear horizontal shrinkage on the top surface and a large temperature difference at 4-5 min (ΔT ~ 300 °C). Thus, this thicker sample was more difficult to bend by the drying shrinkage and thermal expansion of the wood.

When the pyrolysis process became strong at 5-10 min, the wood slice eventually started to bend upward to form a clear ∪ shape, because as the wood converted into char, the effective thickness of the wood layer became smaller. Inconsistent with the 5-mm thick sample, the Stage-III ∪ shape also corresponded to the second peak mass loss. For this 15-mm thick sample, the Stage-IV ∩ shape was as apparent as the 5-min thick sample in Fig. 3a, because the char layer eventually became thin as the smoldering burning continued.

2.3 Effect of size and aspect ratio

Fig. 4 correlates the time of reaching maximum deformation ($t_{\theta,max}$) with (a) the time of reaching local peak mass flux ($t_{m,max}$) and (b) the time of reaching maximum temperature difference ($t_{\Delta T,max}$) under different sample aspect ratios. The time ratio close to 1 means a strong correlation between these two processes, while away from 1 means less relevant. There is a strong correlation between the maximum deformation in Stage I (∪ shape) and the first peak mass flux, the maximum deformation in Stage II (∩ shape) and first peak temperature difference, as well as the maximum deformation in Stage III (∪ shape) and the second peak mass flux.

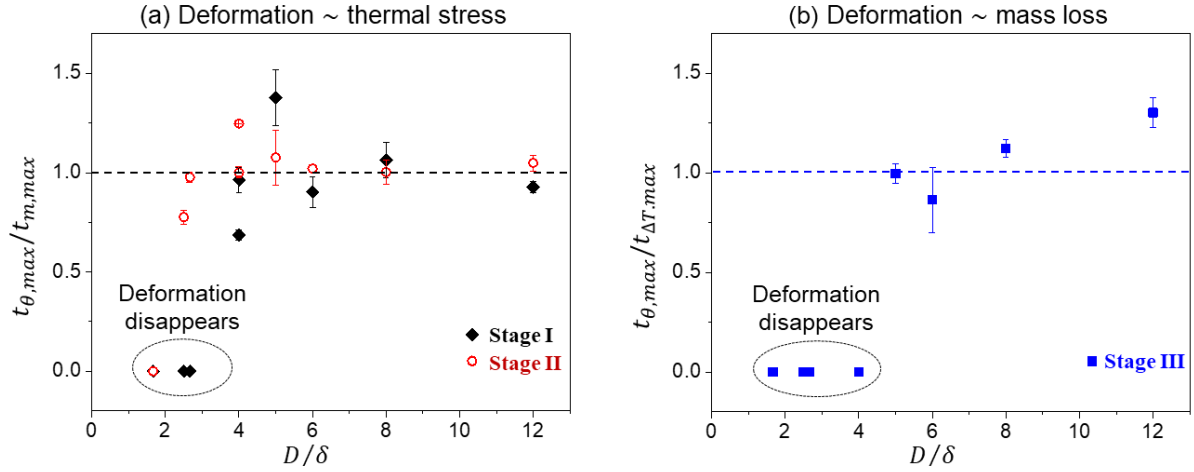

Fig. 4. Effect of aspect ratio (D/δ) on Stages I-III, (a) the time of reaching maximum rotation ($t_{\theta,max}$) to the time of reaching the maximum mass loss rate ($t_{m,max}$) during upward bend to ∪ shape in Stages I and III, and (b) $t_{\theta,max}$ to the time of reaching maximum temperature difference ($t_{\Delta T,max}$) during downward bend to ∩ shape for Stage II.

In Fig. 4, *y* value of 0 indicates the disappearance of the deformation stage; that is, the occurrence of peak mass flux or the temperature difference does not affect the corresponding deformation. The larger aspect ratio (D/δ) means that the sample is slimmer. For the sample with larger D/δ (> 5), four deformation stages can be clearly observed (see Fig. 3a). With $D/\delta \approx 4$, Stage II (∩ shape) disappears. If D/δ further decreases to 2.5~2.67, both stage I (∪ shape) and II (∩ shape) become invisible. Moreover, only Stage IV (∩ shape) can be clearly observed for D/δ=1.67 in Fig. 4. Thus, as D/δ decreases, the sample becomes less slim, and the deformation becomes smaller, where different stages disappear or overlap with each other.

On the other hand, regardless of the sample size and shape, the last deformation Stage IV always exists. Fig. 5 summarizes the effect of sample characteristic size (both thickness and diameter) on (a) maximum temperature difference (ΔT_{max}), and (b) the maximum rotation (θ_{max}) or the maximum deformation in Stage IV. Fig. 5(a) shows that ΔT_{max} is more sensitive to the thickness than the diameter, because the variation of thickness is in the same direction of radiant heat flux and the smoldering propagation. As expected, the temperature difference also decreases as the thickness increases.

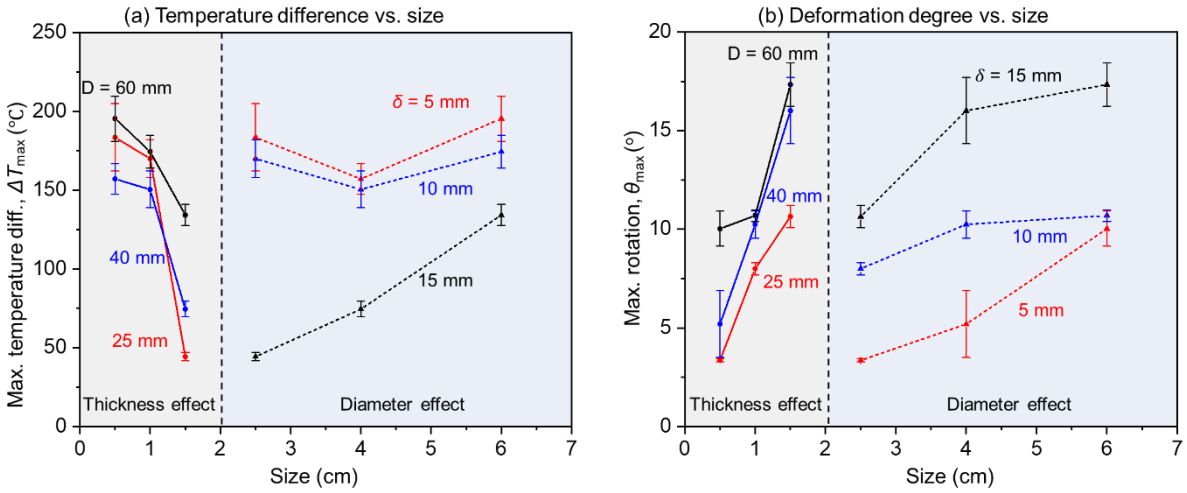

Fig. 5 Diameter/thickness effect on (a) the maximum temperature difference (ΔT_{max}) and (b) the maximum rotation (θ_{max}) of Stage IV.

Fig. 5(b) shows that the degree of deformation in Stage IV increases as the size increases, which is contrary to the trend of deformation in Stages I-III (see Fig. S1 in the Supplemental Material). The deformation in Stages I-III decreases as the size increases because the structural stiffness increases with the increasing thickness or diameter. At the end of Stage IV, ash is the main component of the residue, which has a weak adhesive force. As the thickness of the wood slice increases, the final ash layer is also thicker and heavier, so that the gravity may also contribute to the final rotation.

3. Numerical simulation

3.1 Model setup

To further interpret the burning and deformation processes of wood slices and understand the effects of heterogeneous chemical reactions on stresses and deformation, a simplified 2-D numerical model is established. The details of the numerical model are provided in the Supplemental Materials, and only essential condensed-phase conservation equations of (1) mass, (2) species, and (3) energy are presented

$$\frac{\partial \bar{\rho}}{\partial t} = -\bar{\rho}_0 \dot{\omega}_{fg}''' \tag{1}$$

$$\frac{\partial y_i}{\partial t} = \Delta \dot{\omega}_i''' \tag{2}$$

$$(\bar{\rho}\bar{c})\frac{\partial T}{\partial t} = \nabla\left(\bar{k}\nabla T\right) + \sum_k \bar{\rho}_0 \ \dot{\omega}_k''' \Delta H_k \tag{3}$$

At the top free surface ($z = \delta$), the same irradiation of $\dot{q}''$= 20 kW/m^2 is applied. As the irradiator heats the air, the convective cooling coefficient (h_c) is set to 5 W/m^2-K. The bottom boundary ($z = 0$) faces a cold air with h_c=10 W/m^2-K. The surface re-radiation with a constant emissivity ($\varepsilon = 0.9$) is set for all surfaces. By assuming the thermal equilibrium between gas and solid, the release gases have the same temperature as the solid, and their mass and energy are removed from the domain instantaneously. In the preliminary model, the gas transport was also simulated driven by the Darcy law, and comparison showed that the effect of gas transport on the sample deformation process is very small.

Kinetic model: The heterogeneous chemistry in the smoldering wood fire can be described by a 3-step global kinetic scheme, proposed previously by the thermogravimetric analysis. These three steps are (1) dehydration or drying (*dr*), (2) wood pyrolysis (*py*) and (3) char oxidation (*co*) as

$$\text{wet wood} \rightarrow v_{d,dr}\text{dry wood} + v_{g,dr}\text{H}_2\text{O} \tag{4}$$

$$\text{dry wood} \rightarrow v_{c,py}\text{char} + v_{g,py}\text{gas} \tag{5}$$

$$\text{char} + v_{O_2,co}O_2 \rightarrow v_{a,co}\text{ash} + v_{g,co}\text{gas} \tag{6}$$

where v is the mass stoichiometric coefficient, and subscripts of *w*, *d*, *c, a,* and *g* represent wet wood, dry wood, char, ash, and gas, respectively. Table 1 lists the thermomechanical parameters for all solid species. The average properties of the cell are calculated by using the appropriate mass fraction or volume fraction of each species. The detailed species kinetic parameters are chosen from [26,32,33] (see Table S1 in Supplemental Material). The initial conditions are taken from experimental measurements as

$$y_{w,0} = 1, y_{d,0} = y_{c,0} = y_{a,0} = 0, T_0 = 300K \tag{7}$$

Thermomechanical model: Due to the axial symmetry of the disc wood slice, its deformation can be solved through a 2-D thermo-elasticity equation (i.e., an eigenvalue problem) on a thin elastic layer which is restrained at the central point of the bottom face (Fig. 1). The governing equation of deformation is

$$\nabla\vec{\sigma} + \vec{F}_v = 0 \tag{8}$$

where $\vec{F}_v$ is its overall body load, and the gravity force is the only body force in this model. For the wet wood, the existence of the small amount of bond water creates a volumetric tension force that acts like the pre-tension stress. As the water is released during the drying processes, such a tension force gradually decreases.

The stress tensor of the material ($\vec{\sigma}$) is written according to the Hook's law as

$$\vec{\sigma} = \boldsymbol{C} : (\vec{\varepsilon} - \vec{\varepsilon}_{th}) \tag{9}$$

where the symmetric elasticity ($\boldsymbol{C}$) is a function of the Young's modulus (E_Y) and the Poisson's ratio, and the thermal strain tensor ($\vec{\varepsilon}_{th}$) simulates the influence of thermal expansion. The total deformation

or strain tensor $\vec{\varepsilon}$ can be explicitly written by the displacement $\vec{u}$,

$$\vec{\varepsilon} = \frac{1}{2}[(\nabla\vec{u})^T + \nabla\vec{u} + (\nabla\vec{u})^T\nabla\vec{u}] \quad (10)$$

$$\vec{\varepsilon}_{th} = \alpha\Delta T \quad (11)$$

where the thermal expansion tensor α = 6.67 × 10^{-5} 1/K is set for all species.

Table 1. Physical parameters in model ρ (bulk density), k (solid conductivity), c (specific heat), E_Y (the Young's modulus), where for all species, the Poisson's ratio is 0.4 [26,32,33].

Species	ρ (kg/m^3)	c (J/kg·K)	k $(W/(m\cdot k))$	E_Y (Pa)
wet wood	720	2128.6	0.384	0.5E9
dry wood	650	1900	0.324	0.74E10
char	260	1260	0.2	0.7E7
ash	35	880	0.1	0.5E5

To solve the Cauchy problem (or the displacement field $\vec{u}$), appropriate boundary conditions are assumed. The calculated zone is the free expansion with the initial field $\vec{u}|_{t=0} = 0$, except that the position of the sample bottom center is always fixed like the experiment. All transient equations are customized in the FEA solver of COMSOL. Physical parameters in the model are measured in the experiments or chosen from [26,32,33] (Table 1). The computational domain has the initial cell size of $\Delta z = 0.1$ mm (i.e., 3000 cells), and an initial time step is 0.01 s. Reducing the cell size and time step by a factor of two gives no major difference in modeling results, so calculations are sufficiently resolved.

3.2. Numerical results

Fig. 6 compares the simulated and experimental (Fig. 3a) transient rotation (θ) and temperature profiles (ΔT) of wood slice with a diameter of 60 mm and a thickness of 5 mm. The smoldering ignition of the wood particle is successful for all samples when applying irradiation of 20 kW/m^2 on the top surface. More importantly, all four deformation processes are successfully captured. Note that for such a complex system, the comparison between simulation and experiment is qualitative in nature. The modeled deformation Stage IV occurs later than the experiment, mainly because an average rate is set for the entire char-oxidation reaction, whereas in reality, the char oxidation is faster when the ash layer becomes thinner. Other assumptions, such as the isotropy elastic model and the uniform cooling boundary on the upper surface, also prevent the comparison with experiments at a quantitative level.

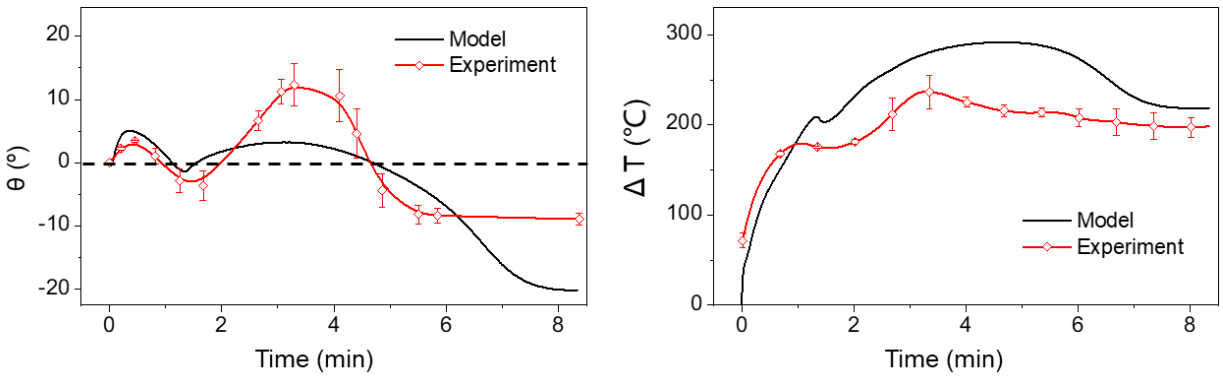

Fig. 6. Comparison of experimental and simulated rotation and temperature difference for a wood slice with the 60-mm diameter and the 5-mm thickness.

Fig. 7 shows the simulated internal stress and deformation pattern of the wood disc with the 60-mm diameter and the 5-mm thickness (also see simulation Videos S3-4). The profiles of temperature, reaction rate, and species mass fraction on the central plane are shown as well. For Stage-I, the upward bending and the drying processes occur at the same time. Moreover, numerical simulations can capture the increasing displacement along with the increasing stiffness and the release of volumetric pre-stress during the drying process. Result reveals that the removal of bond water-induced pre-stress dominates in the drying shrinkage rather than the change in stiffness from wet wood to dry wood.

Stage II corresponds to the largest temperature gradient before the completion of drying, where pyrolysis starts to occur on the top surface. Stage III corresponds to the intense pyrolysis reaction, where the entire wood layer is charred, and the char oxidation starts to occur on the top surface. Stage IV is dominated by strong char oxidation, where the charred sample gradually burns into the ash. Increasing the rate of char oxidation, for example, blowing a wind to increase the oxygen supply and remove the top ash layer, will speed up the final deformation process. Modeling also shows a good stiffness of sample and a negligible gravity (body force) effect throughout the burning. Only near burnout, gravity starts to contribute the downward bend when most of the char is oxidized into ash. Therefore, the established numerical model successfully determines the dominant force and mechanism for different deformation stages, verifies the hypothesis in Section 2.2, and quantified the competitions of the heterogeneous chemistry and thermomechanical stress.

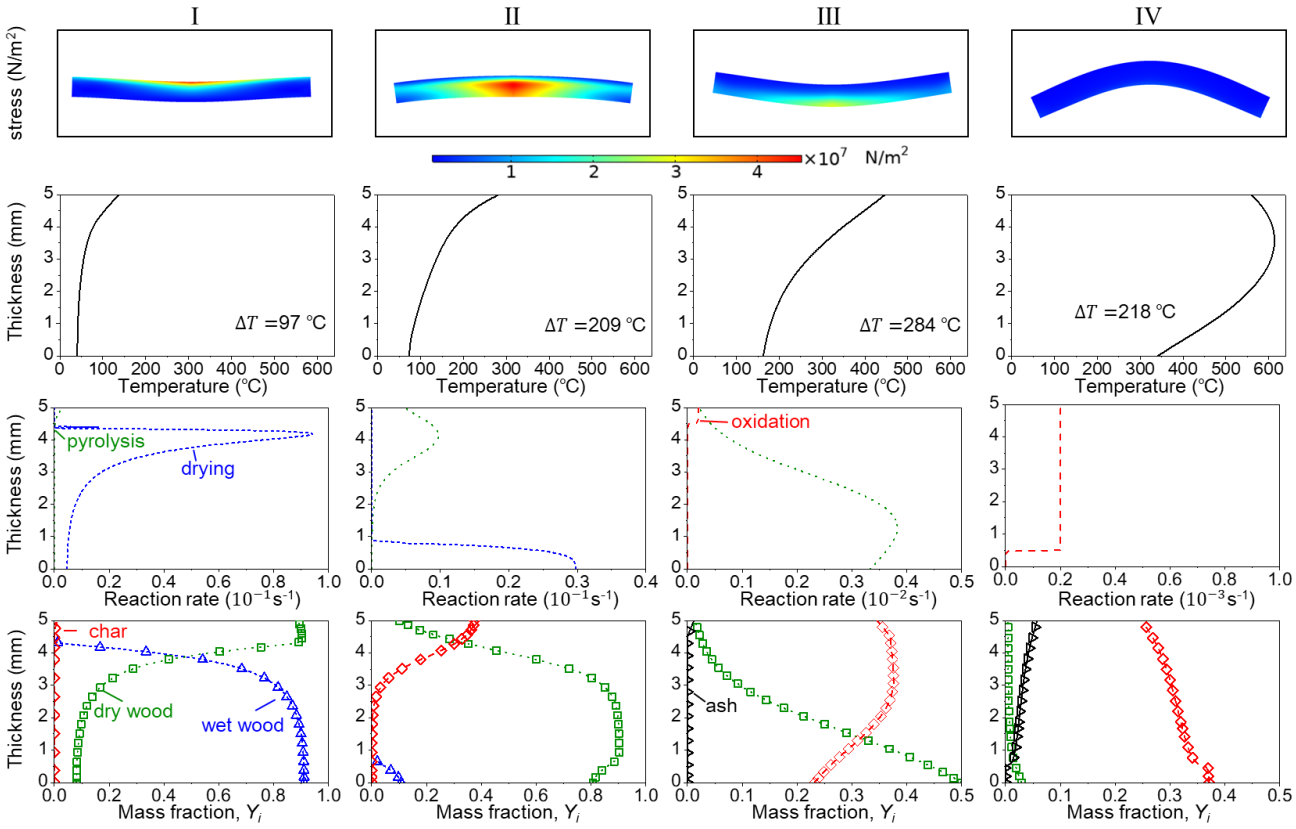

Fig. 7 Simulated deformation processes (Video S3-4) and profile of the temperature, reaction rate and species mass fraction for a wood slice with the diameter of 60 mm and the thickness of 5 mm at the deformation Stage (I) 16.5 s, (II) 78.5 s, (III) 212.5 s, and (IV) 490 s, where the x-axis of reaction rate is adjusted for different stages.

4. Conclusions

In this work, a well-controlled experiment was performed to characterize the smoldering and deformation processes of disc wood slices (diameter of 25-60 mm, thickness of 5-15 mm, and mass of 1.6-26 g) under the irradiation of 20 kW/m^2. The interactions between chemical reactions and thermomechanical stresses lead to four successive deformation stages, (I) drying shrinkage to ∪ shape, (II) irradiation-driven thermal expansion to ∩ shape, (III) pyrolysis shrinkage to ∪ shape, and (IV) oxidation-driven thermal expansion to ∩ shape.

For these 5-15 mm thick slices, the degree and occurrence of these deformation stages are sensitive to the aspect ratio (i.e. D/δ). Increasing the slice thickness decreases the deformation in the first three stages but increases the deformation of Stage IV. These experimental observations are qualitatively reproduced by a 2-D finite-element numerical model, coupling 3-step heterogeneous kinetics with a thermomechanical solver. Modeling results further verified the underlying heterogeneous processes (dehydration, pyrolysis, and oxidation) and thermomechanical stresses (thermal expansion and pre-stress) for each deformation stage. This study helps understand the influence of fire on the deformation of wood and the failure of timber structures.

Acknowledgements

This work is supported by NSFC (51706095, 51876183), Natural Science Foundation of Jiangsu Province of China (BK20171001), China Postdoctoral Science Foundation (2017M611798), HK PolyU (BE-04), and the opening Fund of SKLFS (HZ2017-KF09, HZ2019-KF02).

Nomenclature

c	heat capacity [J/kg K]	α	thermal expansion [1/K]
C	symmetric elasticity	δ	thickness [mm]
D	diameter [mm]	ε	strain tensor [m]
E_Y	Young's modulus [Pa]	θ	rotation [°]
F_V	body load [N]	ν	stoichiometric coefficient [–]
FEA	finite element analysis	ρ	density [kg/m^3]
h_c	conductive coefficient W/(m^2-K)	σ	stress tensor [N/m^2]
k	thermal conductivity [W/m K]	$\dot{\omega}'''$	normalized reaction rate [s^{-1}]
$\dot{m}''$	mass flux [g/m^2 s]		
$\dot{q}''$	heat flux [W/m^2]	*Subscripts*	
t	time [s]	a	ash
T	temperature [°C or K]	c	char
ΔT	temperature difference [°C]	d	dry wood
u	displacement [m]	i	condensed species index
ΔH	heat of reaction [kJ/kg]	k	reaction index
y	mass fraction [–]	s	solid
z	depth [mm]	w	wet wood

References

[1] Song J, Chen C, Zhu S, Zhu M, Dai J, Ray U, et al. Processing bulk natural wood into a high-performance structural material. Nature 2018;554:224–8. doi:10.1038/nature25476.

[2] Chen C, Kuang Y, Zhu S, Burgert I, Keplinger T, Gong A, et al. Structure–property–function relationships of natural and engineered wood. Nat Rev Mater 2020:19–21. doi:10.1038/s41578-020-0195-z.

[3] Emberley R, Inghelbrecht A, Yu Z, Torero JL. Self-extinction of timber. Proc Combust Inst 2017;36:3055–62. doi:10.1016/j.proci.2016.07.077.

[4] Mcallister S, Finney M. Autoignition of wood under combined convective and radiative heating. Proc Combust Inst 2017;36:3073–80. doi:10.1016/j.proci.2016.06.110.

[5] Bartlett AI, Hadden RM, Bisby LA. A Review of Factors Affecting the Burning Behaviour of Wood for Application to Tall Timber Construction. Fire Technol 2019;55:1–49. doi:10.1007/s10694-018-0787-y.

[6] Asdrubali F, Ferracuti B, Lombardi L, Guattari C, Evangelisti L, Grazieschi G. A review of structural, thermo-physical, acoustical, and environmental properties of wooden materials for building applications. Build Environ 2017. doi:10.1016/j.buildenv.2016.12.033.

[7] Barber D. Tall Timber Buildings: What's Next in Fire Safety ? Fire Technol 2015;51:1279–84. doi:10.1007/s10694-015-0497-7.

[8] Manzello SL, Suzuki S, Gollner MJ, Fernandez-Pello AC. Role of firebrand combustion in large outdoor fire spread. Prog Energy Combust Sci 2020;76:100801. doi:10.1016/j.pecs.2019.100801.

[9] Finney MA, Cohen JD, McAllister SS, Jolly WM. On the need for a theory of fire spread. Int J Wildl Fire 2013;2013:25–36. doi:10.1071/WF11117.

[10] Lin S, Huang X, Urban J, McAllister S, Fernandez-Pello C. Piloted ignition of cylindrical widlland fuels under irradiation. Front Mech Eng [under Rev 2019.

[11] Richter F, Rein G. A multiscale model of wood pyrolysis to study the role of chemistry and heat transfer at the mesoscale. Combust Flame 2020;216:316–25. doi:10.1016/j.combustflame.2020.02.029.

[12] Fang MX, Shen DK, Li YX, Yu CJ, Luo ZY, Cen KF. Kinetic study on pyrolysis and combustion of wood under different oxygen concentrations by using TG-FTIR analysis. J Anal Appl Pyrolysis 2006;77:22–7. doi:10.1016/j.jaap.2005.12.010.

[13] Cuevas J, Torero JL, Maluk C. Flame extinction and burning behaviour of timber under varied oxygen concentrations. Fire Saf J 2020:103087. doi:10.1016/j.firesaf.2020.103087.

[14] Richter F, Jervis FX, Huang X, Rein G. Burning rate of wood pyrolysis, smouldering, and flaming: Effect of oxygen. Combust Flame (under Rev 2020.

[15] Lin S, Huang X, Gao J, Ji J. Blue Flame near the Extinction of Wood Fire Part I: An Experimental Study. Fire Saf J (under Rev 2020.

[16] Atreya A, Olszewski P, Chen Y, Baum HR. The effect of size, shape and pyrolysis conditions on the thermal decomposition of wood particles and firebrands. Int J Heat Mass Transf 2017;107:319–28. doi:10.1016/j.ijheatmasstransfer.2016.11.051.

[17] Bilbao R, Mastral JF, Aldea ME, Ceamanos J, Betrán M, Lana JA. Experimental and theoretical study of the ignition and smoldering of wood including convective effects. Combust Flame 2001;126:1363–72. doi:10.1016/S0010-2180(01)00251-6.

[18] Richter F, Kotsovinos P, Rackauskaite E, Rein G. Thermal Response of Timber Slabs Exposed

to Travelling Fires and Traditional Design Fires. Fire Technol 2020. doi:10.1007/s10694-020-01000-1.

[19] Maraveas C, Miamis K, Matthaiou CE. Performance of Timber Connections Exposed to Fire: A Review. Fire Technol 2015;51:1401–32. doi:10.1007/s10694-013-0369-y.

[20] Boonmee N, Quintiere JG. Glowing and flaming autoignition of wood. Proc Combust Inst 2002;29:289–96. doi:10.1016/S1540-7489(02)80039-6.

[21] Boonmee N, Quintiere JG. Glowing ignition of wood: The onset of surface combustion. Proc Combust Inst 2005;30 II:2303–10. doi:10.1016/j.proci.2004.07.022.

[22] Rein G. Smoldering Combustion. SFPE Handb Fire Prot Eng 2014;2014:581–603. doi:10.1007/978-1-4939-2565-0_19.

[23] Keckes J, Burgert I, Frühmann K, Müller M, Kölln K, Hamilton M, et al. Cell-wall recovery after irreversible deformation of wood. Nat Mater 2003;2:810–4. doi:10.1038/nmat1019.

[24] Hori R, Wada M. The thermal expansion of wood cellulose crystals. Cellulose 2005;12:479–84. doi:10.1007/s10570-005-5967-5.

[25] Li K, Hostikka S, Dai P, Li Y, Zhang H, Ji J. Charring shrinkage and cracking of fir during pyrolysis in an inert atmosphere and at different ambient pressures. Proc Combust Inst 2017;36:3185–94. doi:10.1016/j.proci.2016.07.001.

[26] Baroudi D, Ferrantelli A, Li KY, Hostikka S. A thermomechanical explanation for the topology of crack patterns observed on the surface of charred wood and particle fibreboard. Combust Flame 2017;182:206–15. doi:10.1016/j.combustflame.2017.04.017.

[27] Lineham SA, Thomson D, Bartlett AI, Bisby LA, Hadden RM. Structural response of fire-exposed cross-laminated timber beams under sustained loads. Fire Saf J 2016;85:23–34. doi:10.1016/j.firesaf.2016.08.002.

[28] Finney MA, Cohen JD, Forthofer JM, McAllister SS, Gollner MJ, Gorham DJ, et al. Role of buoyant flame dynamics in wildfire spread. Proc Natl Acad Sci U S A 2015;112:9833–8. doi:10.1073/pnas.1504498112.

[29] Li K, Huang X, Fleischmann C, Rein G, Ji J. Pyrolysis of Medium Density Fibreboard: Optimized Search for Kinetic Scheme and Parameters via Genetic Algorithm Driven by Kissinger's Method. Energy & Fuels 2014:140822231738003. doi:10.1021/ef501380c.

[30] Richter F, Rein G. Heterogeneous kinetics of timber charring at the microscale. J Anal Appl Pyrolysis 2019;138:1–9. doi:10.1016/j.jaap.2018.11.019.

[31] Huang X, Li K, Zhang H. Modelling bench-scale fire on engineered wood: Effects of transient flame and physicochemical properties. Proc Combust Inst 2017;36:3167–75. doi:10.1016/j.proci.2016.06.109.

[32] Yapici F, Ozcifci A, Esen R, Kurt S. The effect of grain angle and species on thermal conductivity of some selected wood species. BioResources 2011. doi:10.15376/biores.6.3.2757-2762.

[33] Lautenberger C, Fernandez-Pello C. A model for the oxidative pyrolysis of wood. Combust Flame 2009;156:1503–13. doi:10.1016/j.combustflame.2009.04.001.

[34] Lautenberger C, Fernandez-Pello C. Generalized pyrolysis model for combustible solids. Fire Saf J 2009;44:819–39. doi:10.1016/j.firesaf.2009.03.011.

[35] Lautenberger C. A Generalized Pyrolysis Model for Combustible Solids. 2007.

[36] Huang X, Rein G. Thermochemical conversion of biomass in smouldering combustion across scales: The roles of heterogeneous kinetics, oxygen and transport phenomena. Bioresour Technol 2016;207:409–21. doi:10.1016/j.biortech.2016.01.027.

S. Wang, P. Ding, S. Lin, X. Huang*, A. Usmani (2020) *Deformation of Wood in Fire: The Interaction between Heterogeneous Chemistry and Thermomechanical Stress*, **Proceedings of the Combustion Institute**, https://doi.org/10.1016/j.proci.2020.08.060

Supplemental Materials

The details of the heterogeneous chemistry model are reported here:

$$\frac{\partial \bar{\rho}}{\partial t} = -\overline{\rho_0}\dot{\omega}'''_{fg} \tag{S1}$$

$$\frac{\partial Y_w}{\partial t} = -\dot{\omega}'''_{dr} \tag{S2}$$

$$\frac{\partial Y_d}{\partial t} = \nu_{d,dr}\dot{\omega}'''_{dr} - \dot{\omega}'''_{py} \tag{S3}$$

$$\frac{\partial Y_c}{\partial t} = \nu_{c,py}\dot{\omega}'''_{py} - \dot{\omega}'''_{co} \tag{S4}$$

$$\frac{\partial Y_a}{\partial t} = \nu_{a,co}\dot{\omega}'''_{co} \tag{S5}$$

$$\dot{\omega}'''_{fg} = (1-\nu_{d,dr})\dot{\omega}'''_{dr} + (1-\nu_{c,py})\dot{\omega}'''_{py} + (1+\nu_{O_2,co}-\nu_{a,co})\dot{\omega}'''_{co} \tag{S6}$$

The nondimensional reaction rate of species A is expressed by the Arrhenius law [34]:

$$\dot{\omega}'''_k = Z_k \exp\left(-\frac{E_k}{RT}\right)\left(\frac{m_A}{m_{A0}}\right)^{n_k} \tag{S7}$$

where Z_k and E_k are the pre-exponential factors and the activation energy for reaction k. To simplify the model, the rate of char oxidation is assumed as a constant (0.2×10^{-3} s^{-1}) above a threshold temperature of 400 ℃. The drying process is modeled as a heterogenous reaction (i.e., the dehydration of the wood bond water) in a narrowed temperature region around 100 °C. The detailed species kinetic parameters are chosen from [34–36], as shown in Table S1.

The averaged properties in each cell are calculated, for example, as

$$\bar{\rho} = \sum X_i\rho_i, \quad \bar{c} = \sum X_i c_i, \quad \bar{k} = \sum Y_i k_i, \quad \overline{E_Y} = \sum Y_i E_{Y_i}, \quad X_i = \bar{\rho}\frac{Y_i}{\rho_i} \tag{S8}$$

where X_i is the volumetric fraction of species i, and Y_i is the mass fraction of species i.

Table S1. Chemical kinetic parameters and yields of 3-step reactions for the beech wood. Reaction expression is A $+\nu_{O_2}O_2 \rightarrow \nu_B B + \nu_g$ Gas, and $\Delta H>0$ is endothermic and $\Delta H<0$ is exothermic. [34–36].

Reaction k	Z_k (s^{-1})	E_k (kJ/mol)	n_k (-)	ν_B (-)	ΔH_k (MJ/kg)	ν_{O_2} (-)
Drying	10E10	80	2	0.9	0.205	0
Pyrolysis	3.29E9	135	4.78	0.4	0.533	0
Char oxidation	2E-4	0	0	0.1	−22.31	1.7

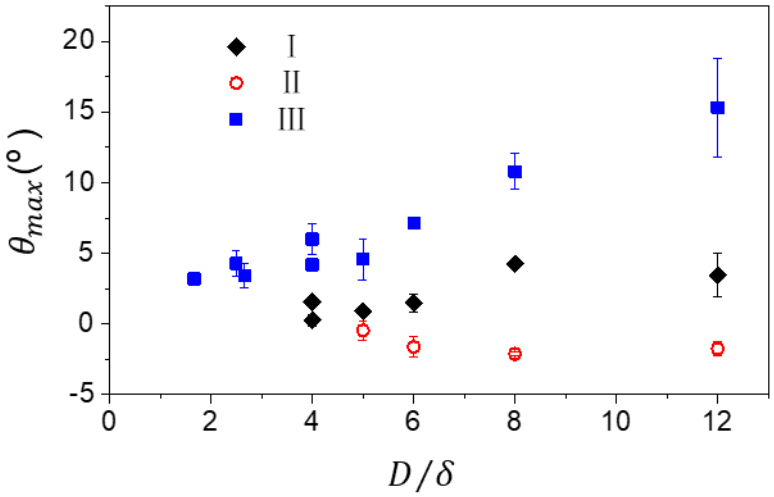

Fig. S1. The maximum rotation (i.e., degree of deformation) of the Stages I-III increases with the aspect ratio (D/δ) of slice, where $\theta > 0$ means a deformation towards the ∪ (or bowl) shape, and $\theta < 0$ means deformation towards the ∩ (or umbrella) shape.